Tellus SERIES A DYNAMIC METEOROLOGY AND OCEANOGRAPHY
PUBLISHED BY THE INTERNATIONAL METEOROLOGICAL INSTITUTE IN STOCKHOLM

Tellus (2010), 62A, 154–169

TELLUS

Horizontal convection in water heated by infrared radiation and cooled by evaporation: scaling analysis and experimental results

By A. K. WÅHLIN[1]*, A. M. JOHANSSON[2], E. AAS[3], G. BROSTRÖM[4], J. E. H. WEBER[3] and J. GRUE[5], [1]*Department of Earth Sciences, University of Gothenburg; PB 460; 405 30 Gothenburg, Sweden*; [2]*Department of Physical Geography and Quaternary Geology, Stockholm University, Sweden*; [3]*Department of Geosciences, Oslo University, Norway*; [4]*Norwegian Meteorological Institute, Oslo, Norway*; [5]*Department of Mathematics, Oslo University, Norway*

(Manuscript received 20 August 2009; in final form 26 November 2009)

ABSTRACT

An experimental study of horizontal convection with a free surface has been conducted. Fresh water was heated from above by an infrared lamp placed at one end of a tank, and cooled by evaporation as the water moved away from the heat source. The heat radiated from the lamp was absorbed in a thin (less than 1 mm) layer next to the surface, and then advected and diffused away from the lamp region. Latent heat loss dominated the surface cooling processes and accounted for at least 80% of the energy loss. The velocity and temperature fields were recorded with PIV technology, thermometers and an infrared camera. In similarity with previous horizontal convection experiments the measurements showed a closed circulation with a gradually cooling surface current moving away from the lamp. Below the surface current the water was stably stratified with a comparatively thick and slow return current. The thickness and speed, and hence the mass transport, of the surface- and the return current increased with distance from the lamp.

The latent cooling at the free surface gives a heat flux which increases with the temperature difference between the surface water and the air above it. Hence the surface temperature relaxes towards an equilibrium value, for which the heat flux is zero. The main new result is a scaling law, taking into account this relaxation boundary condition for the surface temperature. The new scaling includes a (relaxation) length scale for the surface temperature, equivalent to the distance the surface current travels before it has lost the heat that was gained underneath the lamp. The length scale increases with the forcing strength and the (molecular) thermal diffusivity but decreases with the strength of the relaxation. Numerical simulations of this problem for a shallow tank have also been performed. The velocity and temperature in the laboratory and numerical experiments agree with the scaling laws in the upper part of the tank, but not in the lower.

1. Introduction

Horizontal convection is the circulation that arises in a fluid that is heated and cooled at the same pressure level. A natural application is the ocean, which is heated and cooled from the surface. Several experimental studies of non-rotating horizontal convection have been conducted over the past century (e.g. Sandström, 1908; Sandström, 1916; Rossby, 1965; Pierce and Rhines, 1996; Mullarney et al., 2004; Wang and Huang, 2005; Coman *et al.*, 2006; Kuhlbrodt, 2008, and the non-rotating parts of Wells and Wettlaufer, 2008). In all these studies (where differential heating was imposed near the bottom) a closed circulation was obtained in which cold water moved away from the cooling region, and rose as a buoyant plume over the heating region. Scaling for the thickness of the thermal boundary layer and the speed of the water therein was first obtained by Rossby (1965) and later by Mullarney *et al.* (2004) and Wang and Huang (2005). Numerical studies of horizontal convection also show a closed circulation (e.g. Rossby, 1998; Paparella and Young, 2002; Mullarney *et al.*, 2004; Siggers *et al.*, 2004), and confirm the scaling law of Rossby (1965); that the ratio of heat transport by convection and conduction to heat transport by only conduction increases as the Rayleigh number to the one fifth. For large Rayleigh- and/or small Prandtl numbers a transition to unsteady flow occurs (Miller, 1968; Paparella and Young, 2002), which was also observed in the experimental studies by Wang and Huang (2005)

*Corresponding author.
e-mail: awahlin@gu.se
DOI: 10.1111/j.1600-0870.2009.00427.x

and Mullarney *et al*. (2004). However, as shown by Paparella and Young (2002), horizontal convection can not become truly turbulent (in the sense that the dissipation should approach a non-zero value in the limit of zero viscosity).

In the previous studies, the thermal driving force was supplied by differential heating at the base of the tank. This was achieved either through a linear temperature gradient (Rossby, 1965; a similar setup was also used in Wang and Huang, 2005 and Wells and Wettlaufer, 2008), or by a differential heat flux (Mullarney *et al*., 2004). Scaling analysis indicated that the horizontal temperature gradient (or the differential heat flux together with the tank length) thus imposed at the base controls the circulation strength (Rossby, 1965; Mullarney *et al*., 2004).

In this paper, we report a new set of experiments where the differential heating occurs at the free, constant-pressure surface in a laboratory tank. The source of heating in the experiments is the absorption of long-wave radiation in a localized region. In this region the fluid becomes heated and expands, resulting in a surface level rise, and an associated horizontal pressure-gradient force from the warm to the cold region. This tends to drive the fluid away from the warm region, and the motion occurs in a thermal boundary layer near the surface. In the early stages of the process there is no pressure gradient below the warm surface layer, since no mass has been added to the vertical fluid column. But the horizontal advection of fluid in the warm surface layer, and the mass loss due to evaporation in the warm region, eventually generates an adverse pressure-gradient force in the deeper parts that causes a return flow towards the warm region.

The problem of quantifying this circulation is related to the surface thermal boundary condition, which can be of either Dirichlet, Neumann or Cauchy type. The Dirichlet type boundary condition, in which the temperature at the surface is prescribed, was used, for example, in Rossby (1965), Paparella and Young (2002) and Wang and Huang (2005). A Neumann type boundary condition, in which the vertical derivative of temperature (i.e. the heat flux) at the surface is prescribed, was used, for example, in Mullarney et al. (2004) and Spall (2004). In the real ocean, however, the heat flux depends on the surface temperature, or rather the difference in temperature between the atmosphere and the ocean (e.g. Haney, 1971). An alternative surface boundary condition for temperature is that the energy flux (from, e.g. solar radiation) at the surface is specified. This energy flux is balanced both by a heat flux down into the ocean, whereby the deeper water is warmed, and by an energy loss from ocean to atmosphere at the surface. The surface energy loss occurs via latent heat flux, sensible heat flux, and long-wave radiation from the water (Haney, 1971). Since the energy loss at the surface is a function of the sea surface temperature the heat flux becomes a function of the surface temperature, that is, a Cauchy type boundary condition. The heat flux is zero when the surface water is at equilibrium temperature (for which the energy loss equals the specified energy input), and it increases with the difference between the surface water temperature and the equilibrium temperature (Haney, 1971). This, more general, Cauchy type boundary condition can therefore be described as a relaxation condition, in which the surface temperature relaxes towards an equilibrium temperature (see e.g. Haney, 1971; Walin et al., 2004; Spall, 2008; Wåhlin and Johnson, 2009).

In the present experiments heating was supplied by an infrared lamp irradiating the water surface at one end of a tank. Hence the energy flux was specified by the lamp. The water had a free surface which lost heat through evaporation, long-wave radiation and heat conduction. Among these processes latent heat loss via evaporation dominated and balanced at least 80% of the nominal energy input from the lamp. The experimental technique is similar to the process in the ocean, where solar radiation is absorbed at low latitudes and the energy released to the atmosphere at higher latitudes. The majority of this heat loss is latent (Gill, 1982; Haney, 1971). The evaporation rate in our laboratory experiments increased approximately linearly with the surface water temperature and, hence, the relaxation condition for the surface temperature was assumed to be linear. This condition was used together with the governing equations to obtain new scaling laws, most importantly a new relaxation length scale. This length scale describes the distance after which the surface water has reached equilibrium temperature, which in the present experiments was the laboratory room temperature, kept constant to within a degree. The laboratory experiments were complemented with a set of finite element numerical solutions. In the experiments as well as the numerical solutions the surface temperature and velocity behaved according to the scaling. However, the horizontal velocity beneath the thermal boundary layer has a vertical scale that is given by the tank depth. This was shown by assuming a similarity solution for the thermal field, and obtaining an analytical solution for the velocity field.

2. Experimental setup

Figure 1 shows a sketch of the experiment. The experiments were conducted in tanks of inner dimensions length L_{T}, height H and width W. Two different tanks were used, one short with $L_{\mathrm{T}} = 150$ cm and one long with $L_{\mathrm{T}} = 300$ cm (see Table 1). In both tanks the walls and bottom were made of glass, 1 cm thick, that were insulated with 4.8-cm-thick styrofoam plates. In the 300 cm long tank a vertical false wall was inserted in order to change the effective tank length and then three experiments with tank length 300, 200 and 100 cm were conducted. The tanks were initially filled with de-aired water. The heating source, an infrared lamp, was placed above the free surface at one end of the tank. In the short tank a rectangular infrared lamp of dimensions 40×13.4 cm with three different power settings was used, and in the long tank a 40 W ceramic heater was used. Of the infrared radiation incident at the water surface, 6% was reflected (see Appendix A) and the remaining was absorbed by the water. Over 99% was absorbed within the first millimetre of the surface layer

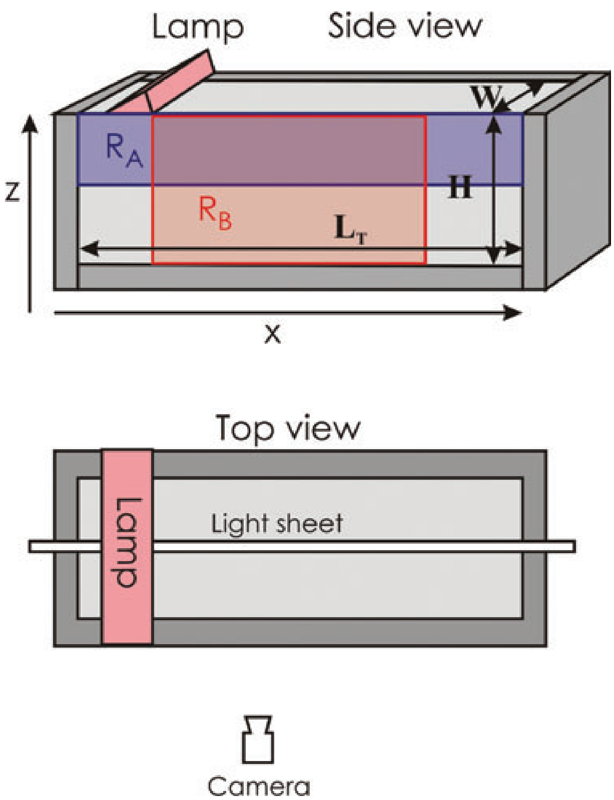

Fig. 1. Sketch of the experiment set-up, some of the notations used and the coordinate system.

(see Appendix A). The heated water left the region below the lamp as a thin, buoyant surface current. As it moved away from the lamp the current cooled, accelerated and thickened. Hence the mass transport in the surface flow increased with distance from the lamp. When it reached the far wall it sank and returned toward the lamp end as a deeper return flow, which slowed down and became thinner as the lamp was approached. Hence there was an upwelling of fluid from the lower layer to the surface layer in the region where the current accelerated. Each experiment was run for 4–9 d, during which time the surface temperature, the interior temperature stratification, and the velocity field was monitored.

Six different experiments with different forcing strength, tank dimension and initial water temperature were conducted (Table 1). The first three experiments were conducted in the 150-cm-long tank, the water was initially at room temperature (24–26 °C, which was kept constant by the air conditioning system), and three different forcing strengths (100, 200 and 300 W) were used. The temperature field as well as the velocity field was recorded daily for these three experiments. The first three experiments were repeated once, and during the repetition runs the surface temperature as well as a second set of velocity measurements were obtained. The last three experiments were conducted in the 300-cm-long tank, with the false wall adjusted

Table 1. List of the experiments and heat loss terms

Exp no.	Q_{lamp} (W)	$T_{INITIAL}$ (°C)	E_0 (W m^{-2})	I_0 (W)	Duration (d)	Evaporation (cm d^{-1})	W (m)	H (m)	L_T (m)	Q_L (W)	Q_{LW} (W)	Q_R (W)	Q_S (W)	Q_H (W)	$\sum Q$ (W)
L1	100	25	1650	66.1	7	0.42	0.4	0.4	1.5	63	5.5	4.3	0–1	29.7	103–104
L2	200	26	3720	149	6	0.78	0.4	0.4	1.5	135	17.2	9.8	1–2	41.6	205–206
L3	300	25	5770	231	5	1.07	0.4	0.4	1.5	185	28.5	15.5	5–10	53.7	288–293
L4	40	16	625	25	8	–	0.15	0.3	3	–					
L5	40	15	625	25	8	–	0.15	0.3	2	–					
L6	40	17	625	25	6	–	0.15	0.3	1	–					

Notes: Q_{lamp} is nominal lamp effect, $T_{INITIAL}$ is initial water temperature in °C, E_0 is downward infrared irradiance transmitted through the water surface, I_0 is the corresponding input of IR radiation, Q_L is latent heat loss, Q_{LW} is energy loss by long-wave radiation from the surface, Q_R is reflected downward IR radiation from the lamp at the surface, Q_H is heat loss from the sides and back of the lamp and Q_S. is heat storage resulting from the increase of the tank water temperature. The sum of the loss terms is shown in the column $\sum Q$.

so that the effective tank length was 100, 200 or 300 cm. The water was initially slightly cooler than room temperature and the forcing strength was 40 W. The surface temperature was photographed daily with an infrared camera, and three temperature loggers recording every 15 s were also placed in the tank. Two of the loggers were in the bottom, one beneath the lamp and one next to the far wall, and one was placed in the surface at the far wall. The infrared camera has an absolute accuracy of 1 °C, which is relevant when comparing different experiments. The relative accuracy, which is relevant when comparing pictures taken from the same experiment, is much higher (0.01 °C) [Flir Technologies]. The accuracy of the temperature loggers is 0.1 °C.

The circulation that developed was mainly two-dimensional and, in the first three experiments, recorded with Particle Image Velocimetry (PIV). High-reflectance particles (50 μm Dantec Polyamid Seeding Particles) were released in the tank by dripping a mixture of water and particles at the lamp end of the tank. The particles were photographed in a 1.2-cm-thick vertical light sheet that was placed in the centre of the tank (see Fig. 1), and the velocities were obtained by analysing subsequent photographs with the MatPIV software (Sveen, 2004). Surface velocity measurements (area R_A in Fig. 1) with enhanced resolution were conducted, dividing the area R_A in Fig. 1 into 16 squares, 11 × 14 cm, that were photographed individually. This gave sufficient resolution to resolve the thin surface boundary layer, but were time consuming and could not be applied to larger areas. The fine-resolution measurements were only conducted once or twice during an experiment. Only data that had a signal-to-noise ratio of 0.9 or larger were used, and hence the error was less than 10%, or 0.01 cm s^{-1}. Later on experiments 1–3 were repeated, and then PIV measurements were conducted in region R_B which was covered in a single photograph. The resolution was not as high as in region R_A but on the other hand sampling was more frequent (daily). The results were identical for the two sets of experiments. For the experiments conducted in the 300 cm tank an estimate of the maximum velocity at the far wall (i.e. at the cool end of the tank) was obtained by dripping dye into the water and measuring the time it took for the dye to drift 20 cm. The measurements were repeated five times, and the obtained average was used. From the standard deviation of the five repetitions it is estimated that the error in this method was around 30%.

The temperature stratification was recorded in the first three experiments by photographing the front glass wall with an infrared camera. The accuracy of this method was investigated in a separate tank with same depth, glass thickness, and insulation as the main experiment. It was found that the infrared images close to the surface was smoothed compared to what was measured with thermal couples. In order to obtain more reliable measurements of the surface temperature the water surface was therefore photographed separately from above in the second set of experiments.

The use of infrared light as heating source is new in this context. It permits heating at a free surface, which also ensures that heating and cooling takes place at the same pressure level. It is also easy to apply and remove without disturbing the flow, and it is comparatively cheap. In the 150 cm tank, evaporation caused the water level to drop about 0.4–1 cm d^{-1} (Table 1), which was easy to measure. Given the evaporation rate the latent heat loss during the time interval dt, Q_L, can be calculated according to

$$Q_L = LS\rho \frac{d\eta}{dt}, \tag{1}$$

where L is the specific latent heat of evaporation, S is the whole tank surface area, ρ is the water density and dη is the thickness of the layer evaporated during the time dt. Using the measured evaporation rate, Q_L was calculated for each experiment in the 150 cm tank (Table 1). The evaporation from the tank accounted for 61–63% of the nominal energy released by the lamp, and for 80–95% of the energy received by the water. Provided the energy balance is similar for the two tanks, the evaporation rate in the 300 cm tank would be less than 1 mm d^{-1} (since the forcing is smaller), which could not be measured accurately. Other energy loss terms include reflection at the water surface, long-wave radiation from the backside of the lamp and the water surface, heat conduction (sensible heat), and storage of heat when the water in the tank is being warmed up. The reflection and radiation terms are calculated in Appendix A and the results are shown in Table 1. The estimated energy loss terms account for all energy released from the lamp within the error of the lamp intensity (relative error of 5% according to the manufacturer). Hence the basic energy balance for the surface water is absorption of the infrared irradiance (after reflection) and heat loss through evaporation. This energy loss accounts for 80–95% of the energy received by the surface water. It should be noted however that heat loss terms that are negligible compared to the surface fluxes may still be comparable to the fluxes in the interior of the tank. For example heat loss through the tank walls may influence the stratification in the deeper parts of the tank, even though it does not influence noticeably the surface boundary layer.

3. Numerical solutions

In order to increase the parameter range the laboratory experiments were complemented with solutions from a numerical model of two-dimensional horizontal convection in which the thermal diffusivity, evaporation rate, and thermal forcing were varied. Three reference numerical experiments with parameters matching those of the laboratory experiments were conducted (see Table 2). Because of CPU limitations the dimensions of the tank were smaller, only 100 cm long and 10 cm deep. The numerical model is based on the finite element PDE solver Femlab®, which solves the stationary, incompressible, non-hydrostatic Navier–Stokes (under the Boussinesq approximation) equations of motion (Comsol Multiphysics). A linear

Table 2. Parameter values and obtained scales for the laboratory (L) and the numerical (N) experiments

Exp no.	E_0 (W m^{-2})	ν (m^2 s^{-1})	κ (m^2 s^{-1})	β (m s^{-1})	T_S (°)	A (m)	δ (cm)	U (cm s^{-1})
L1	1650	1e-6	1.4e-7	$1.5 \times 10^{-5} \pm 0.5 \times 10^{-5}$	26 ± 7	6 ± 3.5	0.9 ± 0.2	1 ± 0.3
L2	3720	1e-6	1.4e-7	$1.5 \times 10^{-5} \pm 0.5 \times 10^{-5}$	60 ± 15	9 ± 5	0.9 ± 0.2	1.4 ± 0.4
L3	5770	1e-6	1.4e-7	$1.5 \times 10^{-5} \pm 0.5 \times 10^{-5}$	90 ± 20	11 ± 6	0.9 ± 0.2	1.8 ± 0.5
L4, L5, L6	1390	1e-6	1.4e-7	$1.5 \times 10^{-5} \pm 0.5 \times 10^{-5}$	22 ± 6	5 ± 3	0.9 ± 0.2	0.9 ± 0.2
N0	10–2000 (30 values)	1e-6	1.4e-7	1.2e-5	0.1–20	0.1–1.5	1.2	0.04–0.6
NI	2000;	1e-6	1.4e-7	1.2e-5	40;	12	1.2	1.2
Reference	4000;				80;	17		1.7
	6000				120	21		2.1
NII	2000;	1e-6	1.4e-7	2.5e-5	20	1.5	0.6	0.6
	4000;				40	0.9		0.9
	6000				60	1		1
NIII	2000;	1e-6	3e-7	2.5e-5	20	7	1.3	1.3
	4000;				40	10		1.8
	6000				60	12		2.2
NIV	2000;	1e-6	1.4e-7	6e-6	80	95	2.3	2.4
	4000;				160	135		3.4
	6000				240	165		4.17
NV	2000;	1e-6	2.5e-8	6e-6	80	3	0.4	0.43
	4000;				160	4		0.6
	6000				240	5		0.7

Notes: E_0 is downward infrared irradiance transmitted through the water surface, ν is the molecular viscosity, κ is the molecular diffusivity of heat, β is the relaxation constant, T_S is the temperature scale obtained from (18), A is the thermal length scale obtained from (23), δ is the thermal thickness scale obtained from (19) and U is the velocity scale obtained from (24). The standard error of 50% in the estimated β gives rise to the error estimates in the scales T_S, A, δ and U.

equation of state (with a thermal expansion coefficient of $\alpha = 2.7 \times 10^{-4}$ K^{-1}) is used. No-slip and no normal flow boundary conditions are used at all boundaries (the experimental observations show that the velocity is zero at the surface, presumably because of the presence of a surface film); the side walls and the bottom are insulated whereas a relaxation boundary condition is used at the surface. Femlab® provides an iterative method to find the steady state solution. As in all finite element solutions the resolution varies in the domain with the finest resolution where the gradients are largest. It was approximately 1 mm at the surface and the far side wall where sinking took place, and decreased with depth.

4. Results

4.1. Temperature and horizontal velocity

Figure 2 shows daily vertical profiles of the temperature for four different sections in the 150-cm-long tank and heating 100, 200 and 300 W, which corresponds to an energy flux E_0 of 1650, 3720 and 5770 Wm^{-2}. The warmest surface water and strongest vertical temperature gradients are found in section I closest to the lamp, and the surface temperature as well as the vertical gradient decreases with distance from the lamp.

Figure 3 shows the time development of the surface- and bottom temperatures at the cool end of the tank over the course of the experiments. These were continuously recorded by the temperature loggers for experiments 4–6, and for experiments 1–3 daily values were extracted from the infrared images. In all experiments the surface layer warms quickly compared to the deeper water owing to the relatively long time for downward heat mixing. In the 200 and 300 W experiments (red and blue markers) the bottom water temperature had not reached steady state when the experiments had to be aborted due to the large evaporation. Steady state in the lower layer is approached on the diffusive timescale $\tau_D = \frac{H^2}{\kappa}$, where H is the tank depth and κ the molecular diffusivity for temperature. Using the experimental values in Tables 1 and 2 it is seen that τ_D is 10 d for experiments 1–3, and 5 d for experiments 4–6. In contrast, the surface layer in all experiments reaches a steady temperature relatively quickly. The analysis below pertains only to the surface layer.

The surface temperature field has a finger-like structure, visible in the infrared photographs of the water surface in Fig. 4. In Fig. 5, the average over the center strip of the infrared photographs has been plotted as a function of distance from the lamp. Also shown in Fig. 5 is the temperature for the three numerical reference experiments with parameters matching those of the first three laboratory experiments. As can be seen, the agreement is reasonable.

Figure 6 shows the velocity profile in the upper 16 cm of the tank in the 150-cm-long tank, together with the three reference

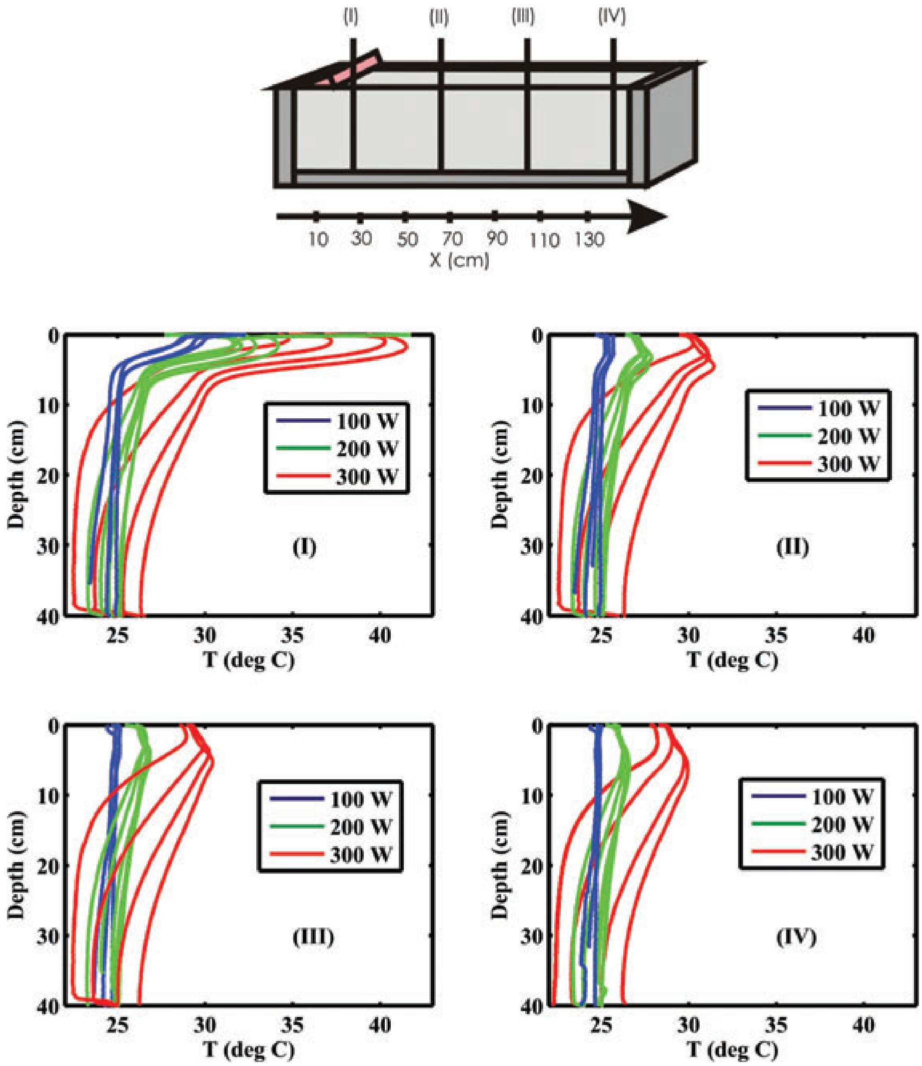

Fig. 2. Laboratory results. Daily vertical profiles of temperature for different forcing strength according to the legend. The four panels correspond to the four sections indicated in the top at distance (I) 10 cm, (II) 50 cm, (III) 90 cm and (IV) 130 cm from the lamp. Time progresses from the leftmost curve and rightward, that is, temperature is lowest initially and increases with time. The accuracy of the measurements is 1 °C.

numerical runs. The warm water leaves the lamp region as a thin surface current, which grows thicker as it moves away from the lamp. The numerical runs and the laboratory experiments have surface currents that are similar both in thickness and magnitude. Below the surface current there is a thicker and slower return flow. The return current in the numerical runs is thinner than in the laboratory experiments, and its velocity is somewhat larger. This may be due to the fact that the numerical runs were performed in a shallower tank than the laboratory experiments, since the return flow thickness scales with the tank depth and not with the thermal boundary layer (see Section 6). Figure 7 shows a time series of the return flow. The resolution in these measurements were however insufficient to resolve the surface current.

4.2. Evaporation rate

The surface boundary condition for temperature is now discussed in some detail. The energy from the lamp is absorbed in a thin surface layer, as shown in Appendix A. The absorbed heat is diffused downward or lost again through the surface. Assume that the dominant heat loss terms per unit area are the latent heat q_L and the net long-wave radiation q_{LW} (W m^{-2}). Then the surface boundary condition for temperature can be written

$$\rho C_P \kappa \left.\frac{\partial T}{\partial z}\right|_{z=0} = E(x) - q_L - q_{LW}, \tag{2}$$

$$E(x) = \begin{cases} E_0 & \text{for} \quad 0 < x < a \\ 0 & \text{for} \quad a < x < L_T, \end{cases}$$

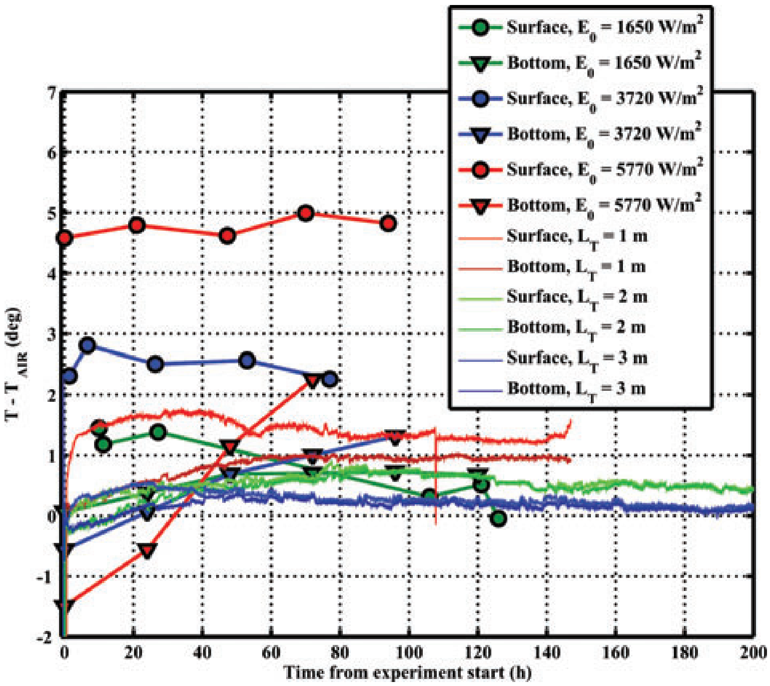

Fig. 3. Surface- and bottom temperature at the cool end of the tank as a function of time for the different experiments according to legend. The accuracy of the measurements is 1 °C for the top six curves, and 0.1 °C for the lower six curves.

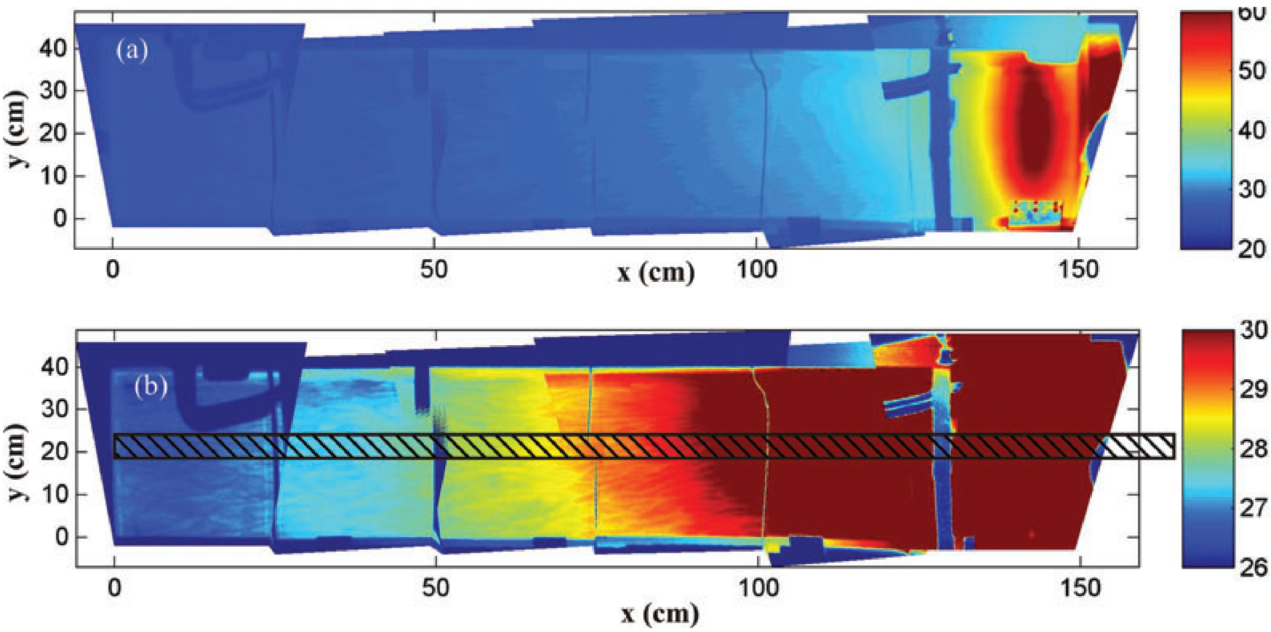

Fig. 4. Surface temperature field. (a) Infrared image showing the surface temperature field, constructed from five separate photographs. Temperature scale according to colour bar. (b) Same as in (a) but with an adjusted colour scale in order to better visualize thermal structures far from the lamp. Hatched region indicates the area over which the averaging was done in Fig. 5.

where $C_P = 4.2$ kJkg^{-1} K^{-1} is the specific heat of water at constant pressure, $\kappa = 1.4 \times 10^{-7}$ m^2 s^{-1} is the molecular thermal diffusivity for water, $E(x)$ (Wm^{-2}) is the infrared downward irradiance in the water just beneath the surface, a (m) is the distance in the x-direction along the tank over which water is heated by the lamp and L_T (m) is the tank length.

The evaporation rate increases with the surface temperature. Figure 8 shows the evaporation rate as a function of the temperature difference between surface water and room air (ΔT). The least squares fit to the data in Fig. 8 gives a slope $r_1 = 2.2 \times 10^{-8}$ (m s^{-1} K^{-1}) that can be used to express q_L as a function of ΔT,

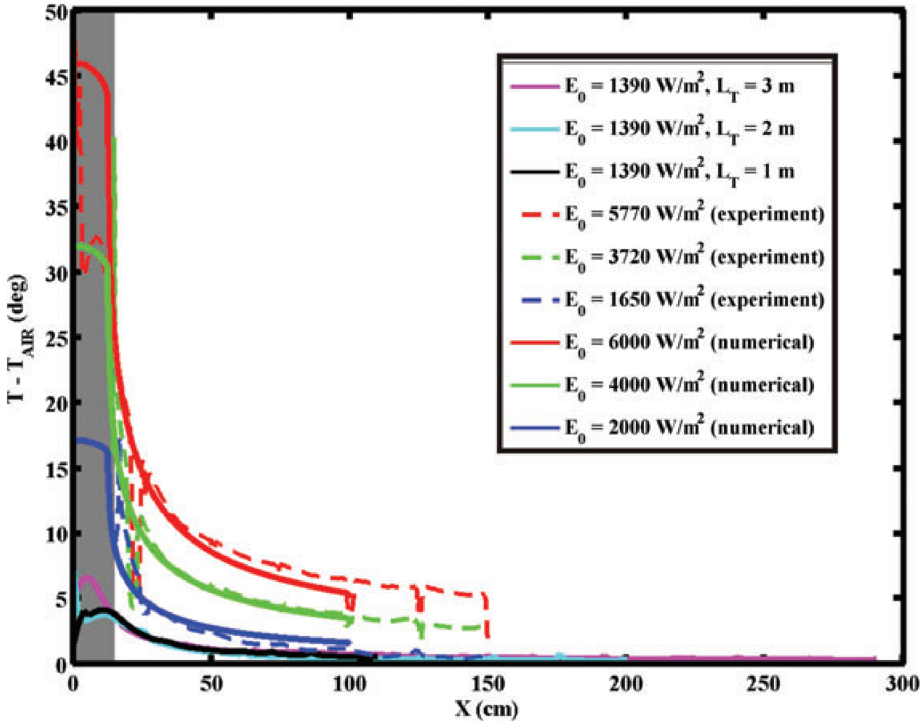

Fig. 5. Surface temperature for the experiments and the three reference numerical solutions (NI in Table 2) according to legend. The dips in the temperature curves are the supportive bars and thin metal rods that were placed above the tank to aid in relating the images to a coordinate system (see Fig. 4). Shaded grey area indicates the location of the heating source, underneath which the infrared imaging is inaccurate. The accuracy of the measurements is 1 °C.

$$q_L = L\rho r_1 \Delta T_{SURF} = r_2 \Delta T_{SURF}, \tag{3}$$

where L is the latent heat of evaporation (2500 kJ kg^{-1}) and $r_2 = L\rho r_1 = 55$ Wm^{-2} K^{-1}. Similarly, the net upward long-wave radiation from the water surface is approximated by linearizing Stefan–Boltzman's law around $T = 25\,^\circ$C,

$$q_{LW} = r_3 \Delta T_{SURF}, \tag{4}$$

where $r_3 = 6.0$ W m^{-2} K^{-1}. Combining (3) and (4), (2) can be written

$$\rho C_P \kappa \left.\frac{\partial T}{\partial z}\right|_{z=0} = E(x) - r_4 \Delta T_{SURF}, \tag{5}$$

where $r_4 = r_2 + r_3 = 61$ Wm^{-2} K^{-1}, or

$$\kappa \left.\frac{\partial \Delta T}{\partial z}\right|_{z=0} + \beta \Delta T\Big|_{z=0} = \frac{E(x)}{\rho C_P}, \tag{6}$$

$$\beta = \frac{r_4}{\rho C_P},$$

where β (m s^{-1}) is a relaxation coefficient and the condition $\frac{\partial T_{ROOM}}{\partial z} = 0$ has been used. According to the experimental data in Fig. 8, β has an error estimated at around 50%.

5. Scaling analysis

The scaling analysis in this section pertains to the surface layer velocity and temperature. The coordinate system and some of the notations used were shown in Fig. 1. Assuming that the flow is two-dimensional, stationary, that the Prandtl number is large, and that the boundary layer approximation can be invoked (i.e. $\frac{\partial}{\partial z} \gg \frac{\partial}{\partial x}$); the equations for momentum, continuity, density and heat are given by (see Rossby, 1965)

$$0 = -\frac{1}{\rho_0}\frac{\partial p}{\partial x} + \nu \frac{\partial^2 u}{\partial z^2} \tag{7}$$

$$\frac{\partial u}{\partial x} + \frac{\partial w}{\partial z} = 0 \tag{8}$$

$$\rho(x, z) = \rho_0\{1 - \alpha[T(x, z) - T_0]\} \tag{9}$$

$$u\frac{\partial T}{\partial x} + w\frac{\partial T}{\partial z} = \kappa \frac{\partial^2 T}{\partial z^2}, \tag{10}$$

where p is the pressure, T the temperature, ρ_0 is the reference density at $T = T_0$ (where $T_0 = 25\,^\circ$C), ν the kinematic viscosity, (u, w) the velocities in the (x, z) directions, α the thermal expansion coefficient ($2.7 \times 10^{-4}\,^\circ$C^{-1}) and κ the molecular diffusivity for heat (1.4×10^{-7} m^2 s^{-1}). The advection term has been neglected in (7).

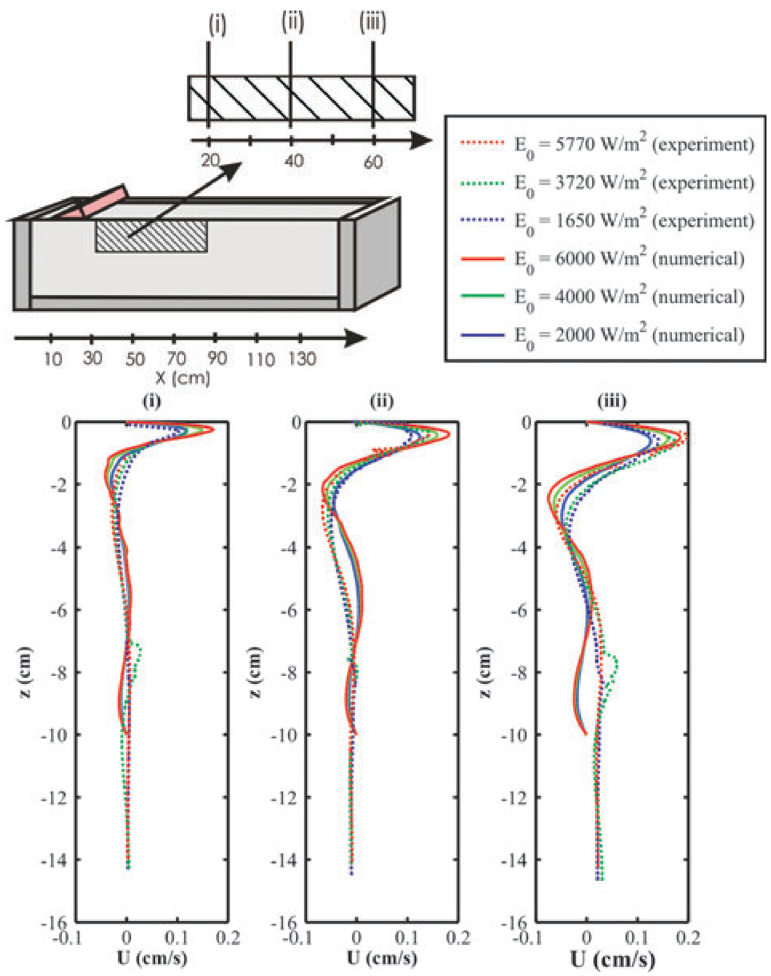

Fig. 6. Vertical plots of the velocity for the experiments and the three reference numerical solutions (NI in Table 2) according to legend. The three panels correspond to the three sections in the top at distance (i) 20 cm (ii) 40 cm and (iii) 60 cm from the lamp. The error of the measurements is 10%.

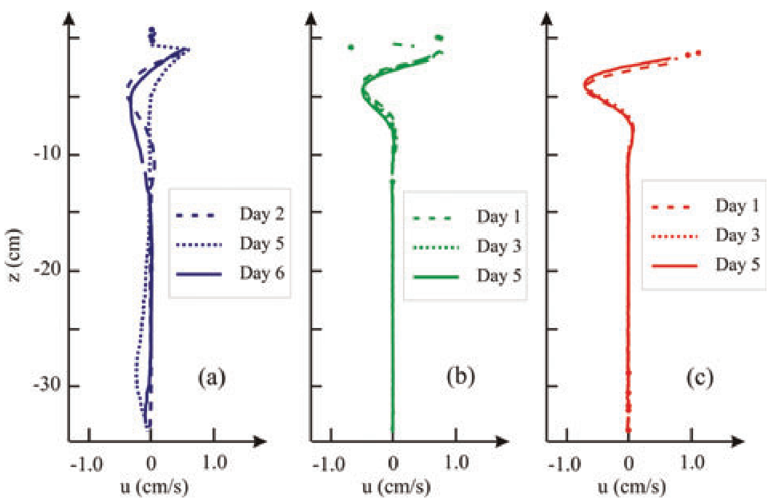

Fig. 7. Coarse-scale velocity measurements from the surface to 35 cm depth in the center of the tank. Line styles indicate time according to legend. (a) $E_0 = 1650\,\mathrm{Wm}^{-2}$, (b) $E_0 = 3720\,\mathrm{Wm}^{-2}$ and (c) $E_0 = 5770\,\mathrm{Wm}^{-2}$. The error margins of the measurements is 10%.

According to (6) the energy which is absorbed underneath the lamp is either diffused downward where it warms the water column or evaporated/radiated away at the surface. In order to get an upper limit of the time when the latent heat loss dominates over diffusion underneath the lamp, it is assumed that the initial time development is governed by the diffusion equation, that is,

$$\frac{\partial \Delta T}{\partial t} = \kappa \frac{\partial^2 \Delta T}{\partial z^2}. \tag{11}$$

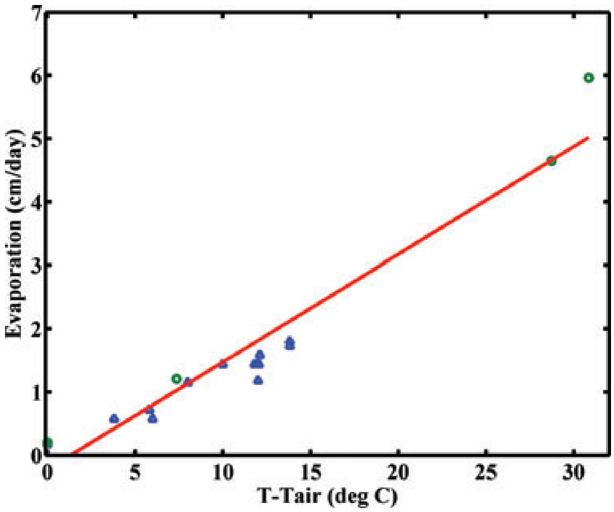

Fig. 8. Evaporation rate as a function of water temperature, measured in a control volume which was kept at different fixed temperatures by use of electric heaters. Triangles and circles are measurements made on two different occasions.

Using the following initial- and boundary conditions,

$$\Delta T(t=0)=0, \quad \Delta T(z=0)=\Delta T_S, \quad \Delta T(z\to\infty)=0, \tag{12}$$

the time development is given by

$$\Delta T(t,z)=\Delta T_S\left[1-erf\left(\frac{z}{2\sqrt{\kappa t}}\right)\right]. \tag{13}$$

From (13) we find for the downward diffusion of heat at the surface

$$\kappa\frac{\partial\Delta T}{\partial z}(t,z=0)=\frac{-\Delta T_S}{\sqrt{\kappa t\pi}}. \tag{14}$$

Immediately after switching on the lamp the downward diffusion of heat dominates over the latent heat loss. However, the temperature gradient at the surface, and thereby the downward diffusion of heat, decreases with time while the latent heat loss increases with time or is constant (after the surface has reached its equilibrium temperature). Hence the latent heat loss at the surface will after a certain time dominate over the heat conduction in (6). By using (14) the two terms in (6) can be compared and it is seen that latent heat loss dominates over diffusion when

$$\frac{\Delta T_S}{\sqrt{\kappa t\pi}}<\beta\Delta T_S, \quad \text{i.e.} \quad t>\frac{\kappa}{\beta^2\pi}. \tag{15}$$

Using the values $\kappa = 1.4\times10^{-7}\,\mathrm{m^2\,s^{-1}}$ and $\beta = 1.5\times10^{-5}\,\mathrm{m\,s^{-1}}$ gives that (15) is true for times larger than 200 s. Since focus is on timescales much larger than 200 s it is assumed that underneath the lamp,

$$\beta\Delta T|_{z=0}=\frac{E_0}{\rho C_P}. \tag{16}$$

Away from the lamp $E(x)=0$, and (6) gives

$$\kappa\frac{\partial\Delta T}{\partial z}\bigg|_{z=0}+\beta\Delta T\bigg|_{z=0}=0. \tag{17}$$

The scale of the surface temperature anomaly underneath the lamp, T_S, and the thermal boundary layer thickness δ follow straight away from (16) and (17), that is,

$$T_S=\frac{E_0}{\rho C_P\beta}, \tag{18}$$

and

$$\delta=\frac{\kappa}{\beta}. \tag{19}$$

If the temperature increases by an amount T_S in a water column of thickness δ, the increase in water level becomes $\Delta\eta=\alpha T_S\delta$. The magnitude of the associated pressure-gradient force that drives the fluid away from the lamp can hence be written (using the hydrostatic approximation)

$$g\eta_x\sim g\frac{\Delta\eta}{A}=\frac{g\alpha T_S\delta}{A}, \tag{20}$$

where A is the horizontal length scale. This force must be balanced by friction, so from (7) we obtain for the velocity scale U in the thermal boundary layer that

$$U=\frac{g\alpha T_S\delta^3}{\nu A}. \tag{21}$$

It should be stressed here that U/δ is the velocity shear near the surface. For the circulation in the entire tank, the horizontal velocity scales with the tank depth H; see the discussion in Section 6. From (8), the vertical velocity scale W in the thermal boundary layer becomes $W=U\delta/A$. Then the heat eq. (10) yields

$$U=\frac{\kappa A}{\delta^2}. \tag{22}$$

Combining (21) and (22), using (19), A becomes

$$A=\frac{\kappa^2}{\beta^2}\left(\frac{g\alpha T_S}{\beta\nu}\right)^{1/2}. \tag{23}$$

The new horizontal length scale A is set by the thermal forcing. It is the natural internal length scale of the problem, and is generally different from the length of the tank used in previous studies. It arises from the conservation of momentum and heat of the problem. From (22) and (23) the near-surface velocity scale is given by

$$U=\kappa\left(\frac{g\alpha T_S}{\beta\nu}\right)^{1/2}. \tag{24}$$

Non-dimensionalizing eqs. (7)–(10), (17) and (20) with the obtained scales we see that ΔT and u scale with T_S and U, and are functions of the dimensionless number $\frac{x}{A}$. In order to compare the different experiments and numerical solutions with the scaling, the maximum velocity 10 cm from the far wall (i.e. at the cool end of the tank), U_{MAX}, and the surface temperature

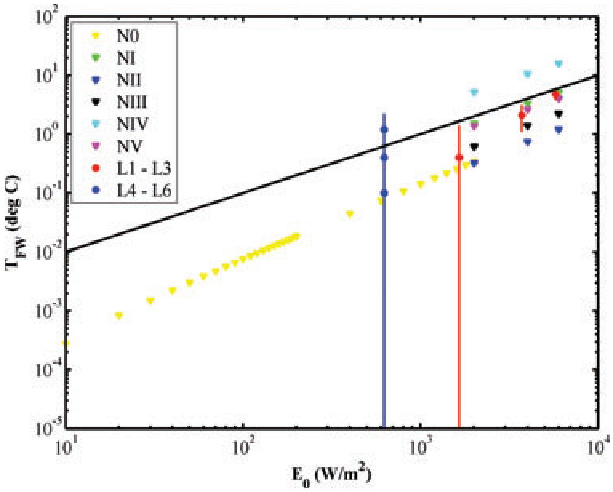

Fig. 9. Surface temperature at the far wall (i.e. at the cool end of the tank) plotted as a function of forcing strength E_0. The markers show values for different numerical solutions (triangles) and the laboratory experiments (circles) according to legend. Parameter values are listed in Table 2. Vertical lines are error bars indicating the accuracy of the temperature measurements. Black solid line shows the linear relationship between the temperature scale and the forcing.

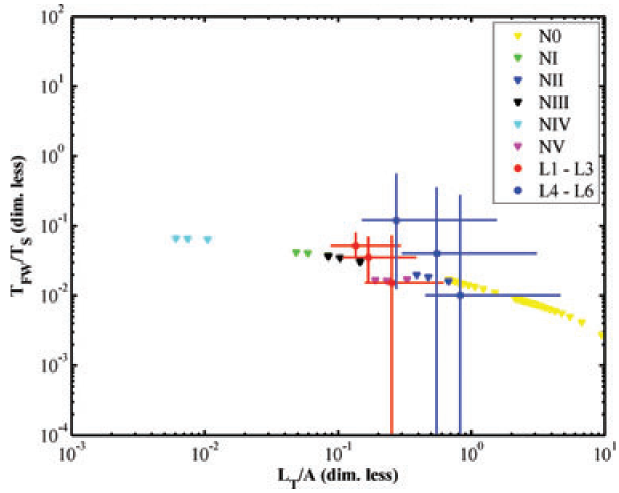

Fig. 10. Surface temperature at the far wall (i.e. at the cool end of the tank), non-dimensionalized with the temperature scale T_S (eq. 18) and plotted as a function of $\frac{L_T}{A}$ where L_T is the tank length and A is the length scale (eq. 23). The markers show values for different numerical solutions (triangles) and the laboratory experiments (circles) according to legend. Parameter values are listed in Table 2. Vertical and horizontal lines are error bars indicating the accuracy of the temperature measurements and the uncertainty in the estimation of A and T_S.

at the far wall, T_{FW}, is used. For the experimental values T_{FW} was defined as the difference between the surface temperature at the far wall and the room temperature. The fluctuations of the room temperature were around 1 °C and when T_{FW} was calculated the temporal mean over the last day of the experiment was used. Figure 9 shows T_{FW} as a function of E_0 for all experiments and numerical solutions. Also inserted is a black line proportional to E_0 in accordance with the scaling (18). The symbols are equal for experiments with equal values of β, κ and tank length and as can be seen most of the numerical experiments behave according to the scaling law when plotted as a function of E_0. For small E_0 the values of T_{FW} increase more rapidly than what is expected from the scaling law. This is because also the length scale A varies with E_0. Since the temperature is a function of the dimensionless parameter $\frac{x}{A}$, it is expected that the data points should collapse to a single line when $\frac{T_{\mathrm{FW}}}{T_S}$ is plotted against $\frac{L_{\mathrm{T}}}{A}$ (using that $x = L_{\mathrm{T}}$ at the far wall). This has been done in Fig. 10, and as can be seen the data points are less scattered than in Fig. 9. The experimental values deviate somewhat from the line described by the numerical solutions. The general decrease of $\frac{T_{\mathrm{FW}}}{T_S}$ with $\frac{L_{\mathrm{T}}}{A}$ is clear but the slope appears to be larger for the experiments. The reason for this can be uncertainties in the estimation of β as well as in the temperature.

Figure 11 shows U_{MAX} as a function of E_0 for the experiments and the numerical solutions. Also inserted is a black line proportional to $\sqrt{E_0}$ in accordance with the scaling (24). In similarity with the temperature, the velocity at the far wall behaves according to the scaling when plotted as a function of E_0. Furthermore the data points collapse to a line when U_{MAX}

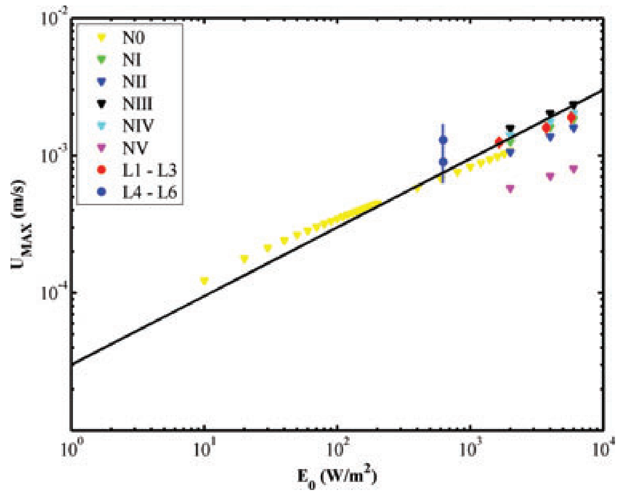

Fig. 11. Maximum velocity at the far wall (i.e. at the cool end of the tank) plotted as a function of forcing strength E_0. The markers show values for different numerical solutions (triangles) and the laboratory experiments (circles) according to legend. Parameter values are listed in Table 2. Vertical lines are error bars indicating the accuracy of the velocity measurements. Black solid line shows the 1/2 power relationship between the velocity scale and the forcing (eqs. 24 and 18).

is non-dimensionalized with U and plotted as a function of $\frac{L_{\mathrm{T}}}{A}$ (Fig. 12), indicating that the general agreement between the data and the scaling theory is good.

Table 2 shows the obtained scales (18, 19, 23, 24) for the six laboratory experiments, and for all the different numerical

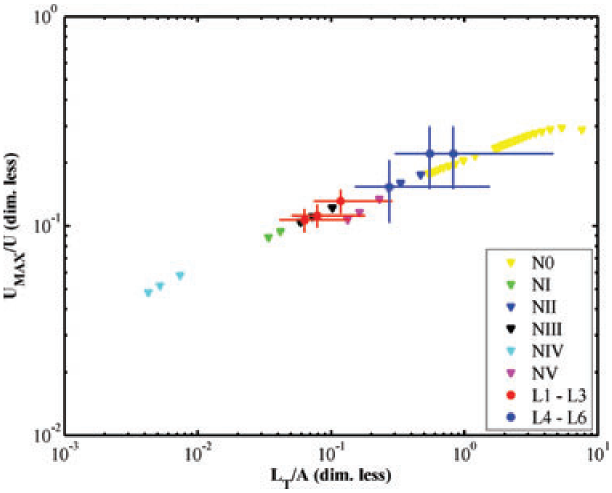

Fig. 12. Maximum velocity at the far wall (i.e. at the cool end of the tank), non-dimensionalized with the velocity scale U (eq. 24) and plotted as a function of $\frac{L_T}{A}$ where L_T is the tank length and A is the length scale (eq. 23). The markers show values for different numerical solutions (triangles) and the laboratory experiments (circles) according to legend. Parameter values are listed in Table 2. Vertical and horizontal lines are error bars indicating the accuracy of the velocity measurements and the uncertainty in the estimation of A and U_S.

solutions (arranged in five groups). In Fig. 12, it appears as if the velocity approaches a constant value for $\frac{L_T}{A} \geq 1$. This value also corresponds to a gradually steepening decline in the temperature as $\frac{T_{FW}}{T_S} \to 0$ (Fig. 10). Hence the length scale A can be interpreted as the distance after which the fluid has lost all the heat it gained underneath the lamp. Even before that limit, at around $\frac{L_T}{A} \approx 0.5$, the temperature anomaly would not have been measurable in the laboratory experiments with the present error margins though.

6. Scaling for the interior velocity

The velocity scaling in previous section only pertains to the surface layer, i.e. the region $-\delta \leq z \leq 0$. Even if the temperature is homogeneous below this layer there can still be a non-zero horizontal velocity, driven by the barotropic pressure gradient force, as explained in Section 1. If we integrate the horizontal momentum equation from the surface to the bottom, it is obvious that we need viscous forcing at the boundaries to balance the motion and obtain a steady circulation. This will occur on a diffusive time scale of order $T \sim H^2/\nu$, and bring in the tank depth H as vertical scaling factor for the horizontal velocity. This can be seen if we postulate that the horizontal temperature gradient has the form (W. R. Young, personal communication, 2008)

$$\frac{\partial T}{\partial x} = -\frac{T_S}{A} e^{\frac{z}{\delta}}. \tag{25}$$

Using the hydrostatic approximation in the vertical, and the equation of state (9), (7) reduces to

$$\nu \frac{\partial^2 u}{\partial z^2} = \frac{g\rho(\eta)}{\rho_0}\frac{\partial \eta}{\partial x} + \frac{g}{\rho_0}\int_z^\eta \frac{\partial \rho}{\partial x} d\xi \approx -C_B - g\alpha \int_z^0 \frac{\partial T}{\partial x} d\xi, \tag{26}$$

where $C_B = -g\frac{\rho(\eta)}{\rho_0}\partial\eta/\partial x$ is the unknown barotropic pressure gradient force that drives the flow away from the lamp. Applying the previous scaling, and inserting from (25), (26) can be written

$$\frac{\partial^2 \hat{u}}{\partial \hat{z}^2} = C_1 - e^{\hat{z}}, \tag{27}$$

where $(u, z) = (U\hat{u}, \delta\hat{z})$ and $(\hat{u}, \hat{z})$ are dimensionless quantities. The general solution to (27) is

$$\hat{u}(\hat{z}) = C_1\frac{\hat{z}^2}{2} + C_2\hat{z} + C_3 - e^{\hat{z}}, \tag{28}$$

where C_1, C_2, C_3 are non-dimensional constants. No-slip conditions for velocity, plus the requirement that there is no net flow through the tank [i.e. $\int_{-H}^0 u dz = 0$] yield

$$\begin{aligned} &\hat{u}(0) = 0 \\ &\hat{u}(-\hat{H}) = 0 \\ &\int_{-\hat{H}}^0 \hat{u}(\hat{z})d\hat{z} = 0, \end{aligned} \tag{29}$$

where $\hat{z} = -\hat{H}$ is the bottom of the tank and $\hat{z} = 0$ is the surface. Then the constants become

$$\begin{aligned} C_1 &= \left(\frac{6}{\hat{H}^2} - \frac{12}{\hat{H}^3}\right)(1 + e^{-\hat{H}}) \\ C_2 &= C_1\frac{\hat{H}}{2} + \frac{1}{\hat{H}}(1 - e^{-\hat{H}}) \\ C_3 &= 1. \end{aligned} \tag{30}$$

If we return to the governing eq. (26) for the horizontal flow, the non-dimensional barotropic pressure-gradient force $C \equiv C_B\delta^2/(\nu U)$ that drives the flow away from the lamp is

$$C = 1 - C_1 \approx 1 - \frac{6}{\hat{H}^2} \approx 1, \tag{31}$$

assuming $\hat{H} >> 1$. The solution (28) (using eq. 30) has been plotted in Fig. 13 for two different tanks with $\hat{H} = 10$ (solid) and $\hat{H} = 35$ (dashed). As can be seen the velocity below the thermal boundary layer has a vertical scale that is similar to the tank depth and not δ. This can also be seen in Fig. 6, where the numerical and experimental velocities are compared. The velocities are similar in the surface, but the return flow occupies a thicker layer in the experiments than in the numerical solution (which was calculated using a shallower tank).

Although the present experiments had a free surface, this surface did not move. This can be seen in Fig. 6 where the velocity approaches zero at $z = 0$. The reason was probably the presence of a surface film that accumulated during the many

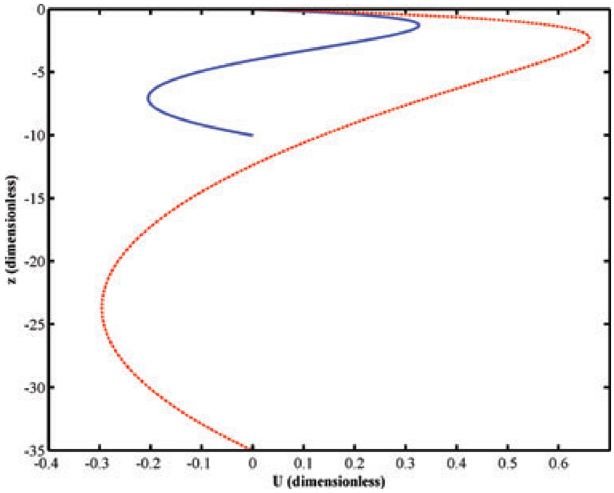

Fig. 13. Analytical solution (31) of the velocity, non-dimensionalized by (24), as a function of the vertical coordinate, non-dimensionalized by $\delta = \frac{\kappa}{\beta}$. Dashed line corresponds to dimensionless tank depth $\hat{H} = 35$, and solid line to $\hat{H} = 10$.

days that the experiment was run. It is not quite clear how this surface film affected the flow. Applying the alternative free-slip condition at the surface, that is, $\frac{\partial u}{\partial z} = 0$ at $z = 0$, the constants $C_1 - C_3$ instead become

$$
\begin{aligned}
C_1 &= \frac{3}{2\hat{H}} - \frac{3}{\hat{H}^3}(1 - e^{-\hat{H}}) + \frac{3e^{-\hat{H}}}{\hat{H}^2} \\
C_2 &= 1 \\
C_3 &= \hat{H} - C_1\frac{\hat{H}^2}{2} + e^{-\hat{H}}.
\end{aligned} \tag{32}
$$

This gives a solution which is quite different from that obtained in (30). In particular, the maximum velocity increases towards infinity when $\hat{H} \to \infty$. The large difference between (30) and (32) suggests that the flow may be very sensitive to the boundary conditions for the horizontal velocity at the free surface. It should however be remembered that the discussion in this section is based on a model for the horizontal temperature gradient which is not an exact solution of the coupled momentum-heat problem.

7. Discussion

In this study, horizontal convection experiments with a free surface have been conducted. Previous experimental studies have not had a free surface, and the heat exchange has taken place through a water–metal surface (Rossby, 1965; Mullarney *et al.*, 2004; Wang and Huang, 2005; Wells and Wettlaufer, 2008). The thermal boundary conditions have either been a prescribed (horizontally varying) temperature (Rossby, 1965; Wang and Huang, 2005), or a prescribed (differential) heat flux (Mullarney *et al.*, 2004). In the present experiments the surface heat flux, mainly latent heat loss through evaporation, increased with the surface temperature. This thermal boundary condition is similar to the relaxation condition described, for example, in Haney (1971), Guan and Huang (2008) and Wåhlin and Johnson (2009), where the surface temperature relaxes to an equilibrium value at which the heat flux is zero. The consequence of the relaxation condition is that the surface water asymptotically approaches room temperature away from the lamp.

In similarity with previous horizontal convection experiments (Rossby, 1965; Pierce and Rhines, 1996; Mullarney et al., 2004; Wang and Huang, 2005), a thermally driven current developed at the surface where the differential heating was supplied. Below this a return flow of colder water took place. The structure and penetration depth of this return flow varies among previous studies as well as in the present. In the experiments by Rossby (1965), Pierce and Rhines (1996), Wang and Huang (2005) and Wells and Wettlaufer (2008), the return flow penetrates the full depth of the tank but the velocity decreases monotonically from a maximum close to the thermal boundary layer to zero at the opposite solid boundary (i.e. the bottom of the tank in this study, and the lid of the tank in previous studies). In the experiments by Mullarney et al. (2004), the return flow consists of a localized current with a velocity maximum close to the tank lid. In the present experiments two return flow structures were observed, (i) a localized cold current at the bottom of the tank (Fig. 7a) and (ii) an intermediate current situated below the warm surface current and above a stagnant body of colder water (Figs. 7b and c). The type (i) structure was observed in experiments 2, 3 and 6, that is, the experiments for which the initial temperature of the tank water was colder than T_{FW} (where T_{FW} is the surface temperature at the far wall). This appears reasonable since the surface water at the far wall feeds the deep current, and hence the deep current will have the temperature T_{FW}. If the water in the bottom of the tank is colder than T_{FW}, the return flow will float above this colder water mass. As shown in Section 6, the scaling derived in this paper only pertains to the surface layer, and the physics behind different penetration depths and structures of the return flow is left for future studies.

Using scaling analysis, and taking the surface relaxation boundary condition into account, a new horizontal length scale was obtained. This internal length scale, A, increases with the thermal forcing and decreases with the relaxation coefficient. In previous studies the thermal boundary conditions have been set so that the tank length has been the appropriate length scale. The present experimental results support the idea that in a tank that is long compared to A the surface will be close to room temperature, with no heat loss and no acceleration of the flow, at some distance away from the heating source. If the tank is short compared to A then the surface water will not have attained room temperature, and it will still be cooling and accelerating, when it hits the far wall. The new length scale A decreases (to the power of 3) with β and increases (to the power of 1/2) with the radiation E_0 and (to the power of 2) with κ. The temperature scale increases linearly with E_0 and decreases as β^{-1}, while the velocity scale increases with E_0 and κ, and decreases with β. The surface temperature at the far wall and the maximum velocity 20 cm away from the wall were non-dimensionalized with the new scales and showed a dependence on the parameter L_T/A, where L_T is the tank length and A the relaxation length, for both experiments and numerical solutions.

Using values pertaining to the ocean, that is, $E_0 = 300\ \mathrm{W\,m^{-2}}$, $\alpha = 2.7 \times 10^{-4}$, $\kappa = \nu = 10^{-5}\ \mathrm{m^2\ s^{-1}}$ (Mullarney et al., 2004) and $\beta = 2 \times 10^{-6}\ \mathrm{m\,s^{-1}}$ gives a temperature scale of 35 °C, a velocity scale of 70 cm s^{-1} and a length-scale of 1740 km. The parameter β can be estimated using the sensible heat flux formula in Gill (1982). Together with a mean wind speed of 5 m s^{-1} and the assumption that the heat flux over the oceans comprises roughly 20% sensible and 80% latent components, this gives a value of $\beta = 2 \times 10^{-6}\mathrm{m\,s^{-1}}$. See also Wåhlin and Johnson (2009) for a discussion of how to estimate β. For the application to the ocean a few things should be pointed out. First, as shown by the analytical solution, the scaling analysis only pertains to the thermal boundary layer. Hence the circulation strength δU should not be interpreted as the Meridional Overturning Circulation (MOC) strength, but rather as the (comparatively) small part of the MOC that actually transports heat towards higher latitudes. Secondly, the thermal forcing in the ocean is highly intermittent and varies on many timescales. There is also more than one source for deep water formation. The presence of these different water masses act to stratify the water column, thus constraining the penetration depth of the subsurface return flow. Perhaps the most important limitation however is posed by Earths rotation. Because of the rotation, currents are steered to the right (in the Northern Hemisphere) and tend to flow along the topography and the coast. When these boundary currents lose buoyancy it does not primarily give rise to a circulation in the meridional-vertical plane, but rather to horizontal gyres that follow bathymetric contours (see, e.g. Mauritzen, 1996; Walin et al., 2004; Spall, 2004; Wåhlin and Johnson, 2009). The results presented here, as well as Sandström's original experiments and other horizontal convection experiments, can be used to assess the strength of the poleward forcing imposed by the differential solar radiation. The fact that the scales obtained match those of the ocean points to the fact that this forcing is not negligible.

8. Acknowledgments

Invaluable technical assistance and building of new constructions were provided by Svein Vesterby. Prof. Knut Jørgen Måløy, Department of Physics, University of Oslo, kindly let us borrow the IR camera. Atle Jensen and Kristian Sveen assisted with the PIV measurements. AW was funded by the Swedish Research Council, for which we are grateful.

9. Appendix: Heating with IR radiation and estimates of heat losses

The lamp was a GLAMOX infrared heater type GVR 505G. While the lamp switch was in the 100 W position the temperature of the heating element was measured by an infrared camera as 593 K. The spectral distribution of the emitted radiation depends on the temperature of the lamp according to Planck's Law, and the spectrally integrated irradiance can be obtained from the Stefan–Boltzmann Law using the emissivity 0.96 for water. The emitted irradiance from the heating element was multiplied by its surface area of 0.0139 ± 0.0004 m^2, and the result became 97.4 ± 2.8 W. The deviation from the nominal 100 W is of the same relative magnitude as the uncertainty of the estimated area. The two other lamp temperatures used in the experiment were 705 K (200 W) and 780 K (300 W).

Not all of the radiation emitted by the heat element will be directed towards the surface of the water. The lamp will absorb some of the heat it produces and suffer heat loss from its sidewalls. A bimetal thermocouple was soldered to the back of the lamp, and its temperature was read off for the different nominal lamp effects. By calculating the long-wave radiation from the Stefan–Boltzmann Law and multiplying it by the area of the sidewalls, the heat losses were estimated to be 29.7–41.6–53.7 W when the nominal effects were 100–200–300 W, respectively. Some heat is also conducted away by the air, probably combined with convection cells in the air above the warmer lamp. Since it is difficult to measure the temperature gradient accurately around the lamp, we have made a very tentative estimate by assuming that the gradient equals the lamp temperature minus the room temperature divided by 10 cm. We have used coefficients for conduction in air presented by Laube and Höller (1988), and our estimate then becomes that the heat loss by pure conduction will be 3.5–3.8% of the loss by long-wave radiation from the side walls of the lamp. If we estimate the temperature gradient by using a length of 1 cm instead of 10 cm, the same heat loss becomes 35–38% of the long-wave radiation from the side wall, corresponding to 10–18% of the loss due to evaporation from the tank. However, we are then most likely overestimating the sensible heat loss, because at a distance of 1 cm from the side wall of the lamp the temperature is definitely higher than the room temperature. Consequently, because of its assumed small magnitude and the difficulty of estimating it accurately, we have neglected the conduction term in the budget of Table 1.

The reflectance of downward irradiance at the surface of the water is a function of the wavelength-dependent refractive index of the water (Lauscher, 1955; Zoloratev and Demin, 1977) and the direction of the downward radiance in air. The IR radiance was assumed isotropic for all downward directions. The resulting spectrally integrated reflectance values became 0.061, 0.062 and 0.063 for the effects 100, 200 and 300 W, respectively. Table 1 shows the heat losses Q_R due to reflection, as well as the inputs I_0 of IR radiation transmitted through the water surface.

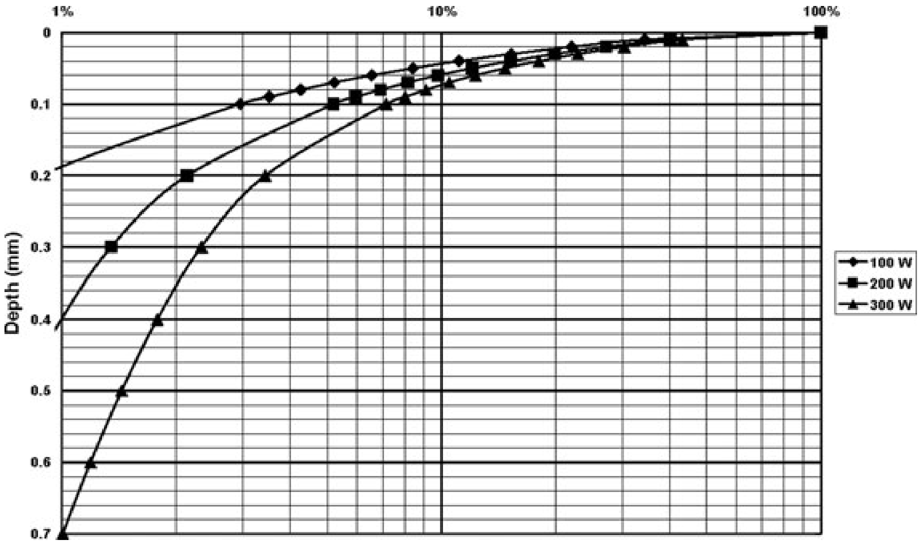

Fig. 14. Remaining energy (in percent of incoming) as a function of depth for the three values of lamp intensity.

In the absence of other processes the absorption of IR radiation would raise the average temperature in the upper 1/10 mm in the tank by 5.4–15.5 K s^{-1}, implying that the water should be boiling within a few seconds, which it clearly does not. This means that the energy will be transported away by other mechanisms. Inside the water body these are downward diffusion and horizontal advection, and at the surface evaporation, long-wave radiation and heat conduction.

The heat loss Q_L due to evaporation was found by measuring the volume of water that had evaporated from the tank during a period, and multiplying the corresponding mass of water with the specific latent heat. The magnitude Q_{LW} of the net long-wave radiation was calculated from Stefan–Boltzmann's Law, using the measured surface temperatures, and reducing the obtained value with the background radiation from the room. The heat conduction (sensible heat) is difficult to estimate, since we are missing accurate values for the temperature gradient above the water surface. Again we have made a very tentative estimate by assuming that the gradient equals the temperature difference between water and room divided by 10 cm. The heat lost by conduction from the water surface becomes 4.4% of the radiation term Q_{LW} in all the different experiments, and we have again assumed that this term can be neglected. The small deviation between the lamp effect Q_0 and the sum of the heat loss terms in Table 1 supports this assumption.

The vertical attenuation of the spectral irradiance $E_\lambda(\lambda, z)$ (W m^{-2} nm^{-1}) with depth z at the different wavelengths can be described by the function

$$E_\lambda(\lambda, z) = E_\lambda(\lambda, 0)\ e^{-K_d(\lambda)\,z}, \qquad \text{(A.1)}$$

where $K_d(\lambda)$ is the vertical attenuation coefficient of downwelling irradiance at the wavelength λ. In the infrared part of the spectrum this coefficient can safely be approximated by

$$K_d(\lambda) \approx a(\lambda)\ /\mu_d(\lambda), \qquad \text{(A.2)}$$

where $a(\lambda)$ is the absorption coefficient of water and $\mu_d(\lambda)$ the average cosine of downwelling radiance in water. We have used values of $a(\lambda)$ for pure water (Curcio and Petty, 1951; Zoloratev and Demin, 1977; Pope and Fry, 1997), although the water in the tank was not particularly clean. However, in the infrared part of the spectrum the absorption coefficient of pure water is so much higher than the coefficient of the pollutants that the latter contribution can be neglected. The average cosine $\mu_d(\lambda)$ is a function of the angular distribution of the transmitted radiances. Since the corresponding transmittances are functions of the refractive index of water which again is a function of wavelength, $\mu_d(\lambda)$ will also vary with wavelength. The average cosine varies in the range 0.73–0.94 with a mean value of 0.84. The details of the calculation of $E_\lambda(\lambda,z)$ in water are presented elsewhere (Aas, 2006). The radiative inputs I_0 presented in Table 1 are obtained by multiplying the spectrally integrated values of $E_\lambda(\lambda,0)$ by the surface area irradiated by the lamp, 0.040 m^2.

Fig. 14 shows how much of the incoming radiation that remains at the different depths. When 1% remains, 99% has been absorbed. As can be seen 99% of the transmitted energy is absorbed within the first 0.2, 0.4 and 0.7 mm at 100, 200 and 300 W, respectively.

References

Aas, E. 2006. Vertical transfer of infrared radiation in water. Univ. Oslo, Dept. Geosciences, MetOs, Rep. No. 129, ISBN 82–91885-33–8.

Coman, M., Hughes, G. and Griffiths, R. 2006. Sandström's experiments revisited. *J. Mar. Res.* **64**(6), 783–796.

Curcio, J. A. and Petty, C. C. 1951. The near infrared absorption spectrum of liquid water. *J. Opt. Soc. Am.* **41**, 302–304.

Gill, A. E. 1982. *Atmosphere-Ocean Dynamics*. Academic Press, San Diego.

Guan, Y. P. and Huang, R. X. 2008. Stommel's box model of thermohaline circulation revisited—the role of mechanical energy supporting mixing and the wind-driven gyration. *J. Phys. Oceanogr.* **38**, 909–917.

Haney, R. L. 1971. Surface thermal boundary condition for ocean circulation models. *J. Phys. Oceanogr.* **1**, 241–248.

Kuhlbrodt, T. 2008. On Sandström's inferences from his tank experiments—a hundred years later. *Tellus* **60A**, 819–836.

Laube, M. and Höller, H. 1988. Cloud physics. In: *Landolt-Börnstein Numerical Data and Functional Relationships in Science and Technology. New Series, Group V Geophysics* Volume 4: Meteorology, Subvolume B Physical and Chemical Properties of the Air. Springer, Berlin, 1–109.

Lauscher, F. 1955. Sonnen- und Himmelsstrahlung im Meer und in Gewässern. In: *Handbuch der Geophysik* Volume 8. Springer, Berlin-Heidelberg-Wien, 723–768.

Mauritzen, C. 1996. Production of the dense overflow waters feeding the North Atlantic across the Greenland–Scotland Ridge. Part 1. Evidence for a revised circulation scheme. *Deep Sea Research I* **43**, 769–806.

Miller, R. C. 1968. *A Thermally Convecting Fluid Heated Non-uniformly from Below*. Unpublished PhD Thesis, Massachusets Institute of Technology, 171.

Mullarney, J. C., Griffiths, R. W. and Hughes, G. O. 2004. Convection driven by differential heating at a horizontal boundary. *J. Fluid. Mech.* **516**, 181–209.

Paparella, F. and Young, W. R. 2002. Horizontal Convection is non-turbulent. *J. Fluid Mech.* **466**, 205–214.

Pierce, D. W. and Rhines, P. B. 1996. Convective building of a pycnocline: laboratory experiments. *J. Phys. Oceanogr.* **26**(2), 176–190.

Pope, R. M. and Fry, E. S. 1997. Absorption spectrum (380–700 nm) of pure water. II. Integrating cavity measurements. *Appl. Opt.* **36**, 8710–8723.

Rossby, T. 1965. On thermal convection driven by non-uniform heating from below: an experimental study. *Deep-Sea Res.* **12**, 9–16.

Rossby, T. 1998. Numerical experiments with a fluid heated non-uniformly from below. *Tellus* **50A**, 242–257.

Sandström, J. W. 1908. Dynamicsche Versuche mit Meerwasser. *Annalen der Hydrographie under Martimen Meteorologie* **36**, 6–23.

Sandström, J. W. 1916. Meteorologische Studien im schwedischen Hochgebirge. *Göteborgs K. Vetenskaps-och Vitterhetssamhalles Handl., Ser. 4* 22(2), 48.

Siggers, J. H., Kerswell, R. R. and Balmforth, N. J. 2004. Bounds on horizontal convection. *J. Fluid Mech.* **517**, 55–70.

Spall, M. A. 2004. Boundary currents and watermass transformation in marginal seas. *J. Phys. Oceanogr.* **34**, 1197–1213.

Spall, M. A. 2008. Low-frequency interaction between horizontal and overturning gyres in the ocean. *Geophys. Res. Lett.* **35**, L18614, doi:10.1029/2008GL035206.

Sveen, J. K. 2004. An introduction to matpiv v.1.6.1. Eprint no. 2, ISSN 0809–4403, Dept. of Mathematics, University of Oslo, http://www.math.uio.no/~jks/matpiv.

Walin, G., Broström, G., Nilsson, J. and Dahl, O. 2004. Baroclinic boundary currents with downstream decreasing buoyancy: a study of an idealized Nordic Seas system. *J. Mar. Res.* **62**, 517–543.

Wang, W. and Huang, R. X. 2005. An experimental study on thermal circulation driven by horizontal differential heating. *J. Fluid Mech.* **540**, 49–73.

Wells, M. G. and Wettlaufer, J. S. 2008. Circulation in Lake Vostock: a laboratory analogue study. *Geophys. Res. Lett.* **35**, L03501, doi:10.1029/2007GL032162.

Wåhlin, A. K. and Johnson, H. L. 2009. The salinity, heat and buoyancy budgets of a coastal current in a marginal sea. *J. Phys. Oceanogr.* **39**, 2562–2580.

Zoloratev, V. M. and Demin, A. V. 1977. Optical constants of water over a broad range of wavelengths, 0.1 Å–1 m. *Opt. Spectrosc*, **43**, 157–161, (U.S. version).